

Multiplexed and millimeter-scale superresolution imaging of cells and tissue sections via prism-illumination and microfluidics-enhanced DNA-PAINT

Matthew J Rames^{1,2}, John Kenison^{1†}, Daniel Heineck^{1,2†}, Fehmi Civitci^{1,2}, Malwina Szczepaniak², Kai Tao², Ting Zheng¹, Julia Shanguan², Sadik Esener^{1,2}, Xiaolin Nan^{1,2}*

1 Cancer Early Detection Advanced Research Center, Knight Cancer Institute, Oregon Health & Science University, 2720 S Moody Ave., Portland, OR 97201, USA.

2 Program in Quantitative and Systems Biology, Department of Biomedical Engineering, Oregon Health & Science University, 2730 S Moody Ave., Portland, OR 97201, USA.

† These authors contributed equally to this work

* Email: nan@ohsu.edu

Abstract

Superresolution microscopy (SRM) has been an enabling tool for biomedical research. A major limitation of SRM, however, is the small field-of-view (FOV), typically $\sim 50\mu\text{m} \times 50\mu\text{m}$ and up to $\sim 200\mu\text{m} \times 200\mu\text{m}$ in recent attempts, hampering its use in imaging large cell populations or clinical tissues. Here we report PRism-Illumination and Microfluidics-Enhanced DNA-PAINT (PRIME-PAINT) for efficient, multiplexed SRM across millimeter-scale FOVs. Unlike existing SRM, PRIME-PAINT uses prism-type illumination for robust DNA-PAINT with single FOVs up to a half millimeter. Through stitching, imaging over mm^2 FOVs can be completed in under an hour per target. The on-stage microfluidics not only facilitates multiplexing but enhances image quality, particularly for tissue sections. We demonstrate the utility of PRIME-PAINT by analyzing $\sim 10^6$ caveolae structures in $\sim 1,000$ cells and imaging entire pancreatic cancer lesions from patient tissue biopsies. Thus, we expect PRIME-PAINT to be useful toward building multiscale, Google-Earth-like views of biological systems.

Introduction

Recent advances in superresolution microscopy (SRM) techniques such as PALM[1, 2], STORM[3], PAINT[4, 5], and STED[6] have pushed the resolution of optical microscopy to 10-20 nm, providing unparalleled insights into biological structures and processes at the molecular scale. However, the high spatial resolution of SRM has traditionally come at a cost to effective FOV compared with prior

diffraction-limited microscopy approaches. At present, most SRM systems (including commercial ones [7]) have an effective FOV around 50 – 100 μm , addressing sample regions equivalent to few cells at a time. This significantly limits the imaging throughput of SRM in studying complex and heterogeneous biological systems, particularly cell populations in model and especially clinical samples that often span millimeters.

Emerging research has begun to push SRM to larger FOVs. High power, homogenous illumination was first used to obtain FOVs of $\sim 200 \mu\text{m} \times 200 \mu\text{m}$ with STORM [8], by employing a total of $\sim 6\text{W}$ lasers ($\sim 640 \text{ nm}$) for efficient photoswitching across such FOVs. Utilizing a line-scanning illumination scheme, Mau et al. have also pushed the FOV of SRM up to $\sim 200 \mu\text{m} \times 200 \mu\text{m}$ with a moderate laser power input ($\sim 250 \text{ mW}$) [9]. The FOVs attained in these methods are still limited to $\sim 200 \mu\text{m}$ in at least one of the dimensions in a large part due to the through-objective illumination and signal collection scheme, which requires the use of high numerical aperture (NA) objectives. Despite the convenience and signal collection efficiency, these schemes afford high quality imaging up to $\sim 200 \mu\text{m} \times 200 \mu\text{m}$, beyond which optical aberrations become limiting. In this regard, methods that can decouple illumination and detection can be more flexible. Indeed, using the coverglass substrate as a waveguide, Archetti et al. achieved FOVs of $>1 \text{ mm}$ (along the direction of light propagation) $\times \sim 200 \mu\text{m}$ (the perpendicular dimension) [10]. This, however, requires strict total internal reflection (TIR) illumination along the entire beam path within the coverglass, and local variations in sample refractive index can lead to beam propagation inhomogeneity and deteriorated image quality. Thus, better optical configurations are still needed to further overcome the current limitations on the achievable FOV in SRM.

Aside from the optical configuration, another important consideration in developing SRM across larger FOVs is the need to image complex biological samples. First, the system design should be fully compatible with and facilitate multiplexed imaging, which is increasingly desired in most biological applications. Current SRM methods – namely PALM, STORM, (DNA-)PAINT, and STED – differ significantly in their approach and capacity to multiplex, of which DNA-PAINT is among the most convenient in terms of multiplexing (through exchange-PAINT [11]). Second, the imaging system should be readily applicable to various sample formats. Most SRM studies are performed on cultured cells for their amenability to high resolution imaging, but clinical, formalin-fixed paraffin-embedded (FFPE) tissue sections are also of immense value in medical research. In fact, SRM with smaller ($50\text{-}100 \mu\text{m}$) FOVs have already shown promises in revealing structural and molecular details from FFPE sections such as chromatin organization in early cancer progression [12] and mitochondria organization [13]. To date, however, none of the existing strategies for large-FOV SRM have been demonstrated on FFPE tissue sections.

To address these needs, we have developed a microscope platform for multiplexed imaging of both cells and clinical tissue samples with DNA-PAINT across up to $\sim 0.5 \text{ mm} \times 0.5 \text{ mm}$ FOVs in a single acquisition. This platform, which we term PRism-Illumination and Microfluidics-Enhanced (PRIME-) PAINT, utilizes a prism-based illumination scheme and affords FOVs much greater than previously achieved using through-objective configurations without sacrificing spatial resolution. Multiplexed SRM imaging via exchange-PAINT is facilitated by the use of an integrated microfluidic sample chamber, which also enabled high quality imaging of clinical FFPE tissue sections via microfluidics enhanced DNA-PAINT. Built upon these, we demonstrate multicolor imaging of both cultured cells and clinical, FFPE sections with nanometer spatial resolutions. Enabled by the dramatically increased data throughput, we used machine learning-based image segmentation and quantitation of the resulting, multiscale SRM images, offering proof of principle insights into nanostructures and molecular interactions across larger cell populations. Collectively, we present PRIME-PAINT as a novel approach to enable high-resolution, high-throughput spatial mapping of cells and clinical samples across the scales from molecules to multicellular systems.

Results

Integrating prism-type illumination and microfluidics for PRIME-PAINT

PRIME-PAINT combines a prism-type illumination scheme with an on-stage microfluidic system for programmable fluid exchange. This combination was essential to enabling multiplexed SRM via exchange-PAINT over much larger FOVs compared with prior configurations. We chose DNA-PAINT as the primary SRM method in this work because of its convenient multiplexing, robust multi-FOV stitching. In this work, we specifically used DNA-PAINT-ERS, our improved implementation of DNA-PAINT, where the combination of ethylene carbonate (EC, as an imaging buffer additive), repetitive docking sequences, and a spacer between the affinity agent and the docking strand (DS) oligo enables fast and high-quality DNA-PAINT without needing strong laser excitation [17].

Prism-based illumination predates the now more popular through-objective scheme. Both are compatible with total internal reflection (TIR) and highly inclined laminar optical (HiLo) imaging modes for objects at the interface and those further inside, respectively. Of the two, the prism-based scheme allows for more tunable large field illumination simply by adjusting the size of the incident laser without being limited to $\sim 200 \mu\text{m} \times 200 \mu\text{m}$ by the high numerical aperture (NA) lens used in through-objective TIR. The scheme also avoids focusing of high lasers onto sensitive optical surfaces (e.g. the back focal plane of the objective lens) and thus can accommodate more incident power if needed [14] (**Fig. 1A**). A rotating mirror, directly before a cage-mounted 4π lens pair, maintains the beam position on the sample when adjusting the incident beam angle to switch between TIR and HiLo imaging modes.

Signals generated near the top glass (coverslide) - solution interface travel through the solution and the coverglass below before being detected by an objective placed at the bottom (**Fig. 1B**). With sample illumination decoupled from signal detection, we could now choose objective lenses best suited for single-molecule detection across large FOVs instead of being constrained to the high NA (typically >1.45) oil immersion lenses used in previous work for both illumination and detection. For this purpose, we found that a 40x silicone (Sil) immersion objective (NA 1.25) [15] outperformed the more commonly used 60x oil immersion (NA=1.4) objective in prism-based illumination setups. Despite the somewhat lower NA, the Sil lens yielded better single-molecule brightness (**Supplementary Fig. S1**) and exhibited superior field flatness than the latter, affording high quality single-molecule imaging across FOVs at $\sim 0.3\text{mm} \times 0.3 \text{mm}$ (**Fig. 1C**, with the Prime 95B sCMOS camera) and even $\sim 0.5\text{mm} \times 0.5\text{mm}$ (**Supplementary Fig. S2**, with the Kinetix sCMOS camera). The switching between the two FOVs only requires adjustment to a variable beam magnifier in the illumination path (**Fig. 1A**) and the camera port.

This imaging strategy necessitated samples be sandwiched between a glass coverslide and a coverglass with the space in between filled with imaging buffer. We designed a microfluidic flow cell with a tear-drop shape for efficient and complete buffer exchange, which is beneficial to multiplexed DNA-PAINT, modeled similarly to other expansion/contraction designs [16]. Fire-polished glass coverslides yielded minimal background autofluorescence and could be directly used with conventional tissue cell-culture or coated with polyethyleneimine (PEI) for use with FFPE tissue sections (see methods). In the final assembly, we used stretched, cut, and melted parafilm as a thin ($\sim 35 \pm 5 \mu\text{m}$ thickness) but robust microfluidic seal. An optional, custom microfluidic exterior holder (see CAD file, **Supplementary software**) positions the sample on the microscope stage to ensure mechanical stability. Finally, inlet and outlet fluid ports were connected to both a computer controlled rotary valve and a peristaltic pump, allowing programmable fluid exchange during imaging (see **Supplementary software**).

Multiplexed PRIME-PAINT for membrane and cytosolic targets in cell populations

High-quality single molecule imaging on the setup enabled large-field, SRM imaging of cellular targets in cultured cells with single FOVs of ~ 0.3 mm x 0.3 mm (**Fig. 2**) or even ~ 0.5 mm x 0.5 mm (**Supplementary Fig. S3**) with PRIME-PAINT. Imaging can be altered between membrane (such as caveolin; **Fig. 2A-D**) and cytosolic (such as mitochondria; **Fig. 2E-H**) targets by switching between TIR and HiLo imaging modes, respectively. The acquisition time for each single FOV of either size was typically 5-20 min (target dependent) owing to the improved imaging kinetics in DNA-PAINT-ERS [17].

We estimated the effective resolution of PRIME-PAINT by measuring the width of microtubules, which should be around 40 nm considering the inherent width and the size of the antibodies and the attached DS oligo). Microtubules exhibited Full Width Half Maximum (FWHM) of 47 ± 3 nm (objective-type DNA-PAINT-ERS) and 51 ± 4 nm (PRIME-PAINT at 0.3 mm x 0.3 mm FOV; see **Supplementary Fig. S4**). These correspond to an effective resolution of ~ 25 nm for the objective-type DNA-PAINT, consistent with our previous results [17], and slightly lower (~ 30 nm) for PRIME-PAINT at 0.3 mm x 0.3 mm FOV using the Prime95B camera. Imaging with the largest 0.5 mm x 0.5 mm single FOVs further lowered the resolution to 40 - 45 nm (FWHM ~ 60 nm; **Supplementary Fig. S4**), primarily due to the lower power density at such large FOVs, and using a laser with 2-3W power output (currently ~ 1 W @ 640 nm) would improve the resolution to the 20 - 30 nm range. A practical challenge for imaging at the larger FOVs is the need to perfectly level the sample such that the entire FOV is in the same focal plane, which is more difficult with the Kinetix. For these reasons, we primarily used the 0.3 mm x 0.3 mm FOV in this work.

The use of DNA-PAINT allowed robust stitching of multiple FOVs to address even larger sample areas. In **Fig. 2A**, we demonstrate a 4×4 stitching (with a ~ 40 μ m overlap) with a combined FOV of 1 mm² in 2-3 hours (10-15 min per single FOV and when imaging mitochondria, and **Fig. 2E** a 3×3 stitching with a combined FOV of 0.8 mm² in 1-2 hours when imaging caveolae, exemplifying the substantial range of spatial and target specific information obtainable by PRIME-PAINT. Leveraging the larger 0.5 mm x 0.5 mm FOV enabled imaging of ~ 1 mm² through 2×2 stitching in under 40 minutes (**Supplementary Fig. S3**). Imaging of the same 1 mm² FOVs would have taken 1-3 days if using DNA-PAINT with the standard FOV or 6-8 hours even with the most recent scanning-based large-field STORM (termed ASTER) [9]. Thus, the PRIME-PAINT approach combined with DNA-PAINT-ERS [17] represents a substantial increase in imaging throughput compared with existing strategies.

The integrated microfluidics (**Fig. 1C**) facilitated multiplexed PRIME-PAINT imaging by allowing hands-free, programmable buffer exchange. As proof-of-principle, we labeled microtubules, mitochondria, and vimentin in cultured COS7 cells and imaged the three targets sequentially using exchange-PAINT (**Fig. 3A & B**). In the co-registered multitarget images all three targets were well resolved, revealing their spatial relationships such as occasional associations between mitochondria and the two cytoskeletal filaments (**Fig. 3C, D**). We similarly obtained a two-target PRIME-PAINT image of microtubules and vimentin over the larger, 0.5 mm x 0.5 mm FOV by switching to the Kinetix camera (**Fig. 3E-G**). A quick washing step between the imaging cycles by flowing in a blank imaging buffer (e.g. PBS with 15% EC) eliminated any residual localizations without noticeable effects on imaging quality (**Supplementary Fig. S5**).

Machine learning based segmentation and quantitation of PRIME-PAINT images

By significantly improving the imaging throughput of SRM, PRIME-PAINT offers unique opportunities to analyze protein localizations and biological nanostructures at the cell population scale, but these vast image datasets also necessitate scalable image analysis tools. In this work, we took advantage of WEKA[18], an open-source platform for machine-learning with a built-in plugin for Fiji[19], for automated identification and analysis of nanostructures from PRIME-PAINT images.

Hundreds of user-defined regions of interest (ROIs), each featuring a single nanostructure, were manually annotated and used for model training, and the model was subsequently applied to unannotated images for identifying features of interest. As reconstructed PRIME-PAINT images were massive (~30,000 x 30,000 pixels when rendered at 10 nm/pixel for images obtained from a single ~300 μm x 300 μm FOV), we developed a Fiji macro to divide, classify, recombine and ultimately quantify nanostructures of interest from PRIME-PAINT images (**Supplementary Fig. S6**, also see Methods).

We illustrate this pipeline by analyzing caveolae in U2OS cells by imaging caveolin-1 with PRIME-PAINT (**Fig. 4A**). WEKA training using ~100 manually segmented structures resulted in a model that recognizes annotated test images with a DICE similarity coefficient of $84\% \pm 8\%$, validating the performance of the trained model (**Fig. 4B**), as also demonstrated by mapping the classification result onto the original PRIME-PAINT image (**Fig. 4C**). Smaller (< 20 nm) puncta were beyond our resolution limit and omitted from this analysis. This allowed us to extract all caveolae from a large number of cells and perform analysis on their abundance, size, localization density, and other properties.

We next applied this model to analyze caveolae in U2OS cells with and without mutant KRas (G12D) expression, as we initially observed that U2OS cells that express higher levels of mutant KRas (KRas^{G12D}) showed an apparently lower abundance of caveolae (**Fig. 5A**). The cells were engineered to express SNAP-KRas^{G12D} upon doxycycline (dox)-induction [20], where SNAP-KRas^{G12D} was labeled using DNA oligo-conjugated SNAP substrate (see Methods) for DNA-PAINT imaging. We then obtained dual-target PRIME-PAINT images of mutant KRas and Caveolin-1 across 12 FOVs (~0.3 mm x 0.3 mm), of which 10 were from cells induced with Dox (KRas^{G12D} positive) and from 2 uninduced (KRas^{G12D} negative). Each FOV contained ~50-100 cells, and the boundaries of all 925 cells were manually annotated to facilitate subsequent quantitation. From these cells, a total of over 630,000 caveolae were extracted, and individual caveolae attributes (area, intensity, diameter) were analyzed.

The analysis indicated an overall perturbation in the caveolae assembly as a result of KRas^{G12D} overexpression. While the total number of caveolae per cell was significantly lower in cells expressing KRas^{G12D}, the average expression level of Caveolin-1 per cell (as measured by the number of DNA-PAINT localizations in the Caveolin-1 channel) only decreased minimally upon KRas^{G12D} induction (**Fig. 5B**). Notably, in all cases (e.g. uninduced cells), there were clearly two populations of caveolae with distinct diameters at ~54 nm and ~154 nm. The two populations may be attributed to fully formed caveolae (~60 nm diameter) and precursor ‘plaques’ (~150 nm diameter) previously identified in EM images [21]. As KRas^{G12D} expression level increased, the sizes of the two caveolae species remained largely unchanged (**Supplementary Fig. S7**) but the percentage of the larger caveolae noticeably decreased (**Fig. 5C**). This observation indicates that mutant KRas expression may promote caveolae maturation (thus more caveolae with ~60 nm diameter), echoing previous reports on the interplay between caveolae and mutant KRas [22, 23], although the effect appeared cell-line and context specific.

While a full validation of this result and its mechanistic interpretation warrant a more extended study, this example demonstrates the feasibility in utilizing PRIME-PAINT in combination with machine-learning based image segmentation in probing alterations in nanoscopic structures across large cell populations, which would have been difficult if not for both the SRM resolution and the larger FOVs.

Optimizing PRIME-PAINT on tissue sections

With cell-based PRIME-PAINT demonstrated, we next sought to apply the imaging platform to clinical FFPE sections. An advantage of tissue DNA-PAINT would be the ability to reliably stitch multiple fields of view without the negative impact of photobleaching from methods like STORM (**Supplementary Fig. S8A-C**). A major issue with DNA-PAINT imaging of FFPE tissue sections, however, was the noticeably lower image quality compared to that of cells (**Supplementary fig. S8D &**

E), even though the targeted structures were well labeled (as confirmed by signal from Cy3 attached to the DS oligos). This contrasts our previous tissue STORM results [13] and suggests that inefficient DS-IS hybridization may be the primary culprit.

When imaging tissue sections with PRIME-PAINT, we observed that the localization kinetics was drastically better when the imaging buffer was still being flown in than when the flow has stopped (as in a normal imaging session) (**Supplementary Fig. S9A**). This suggested that the presence of flow may help improve localization kinetics in tissue PRIME-PAINT and prompted us to systematically investigate this. In fact, a weak flow at 1 $\mu\text{L}/\text{min}$ already increased the observed localizations by ~ 10 -fold and resulted in significantly better resolved structures (**Supplementary Fig. S9B & C**). No obvious additional benefits were evident when the flow rate was increased to 5 $\mu\text{L}/\text{min}$. Thus, the integrated microfluidics addresses the challenge in poor localization kinetics of DNA-PAINT on tissue sections and significantly enhanced the image quality (hence the term PRIME-PAINT) at a negligible cost of 10-20 μL extra consumption of imaging buffer. The addition of flow during imaging also helps imaging of cells under certain conditions (**Supplementary Fig. S10**).

We also introduced other, empirical optimizations to further improve PRIME-PAINT imaging of FFPE tissue sections. First, we found optimal EC% for tissue imaging to be between 5-8% EC (unlike cell imaging at 10-15%) (**Supplementary Fig. S11**), which is perhaps related to refractive index matching between the EC solution and different samples [24]. Second, we found that the combination of Signal Enhancer (SE), a commercial product already used in our previous DNA-PAINT-ERS samples [17], with rNase A treatment during blocking (prior to primary antibody incubation) yields best quality PRIME-PAINT images from tissue sections (**Supplementary Fig. S12**). Collectively, optimal EC concentration $\sim 7\%$ with a 1 $\mu\text{L}/\text{min}$ flow rate on both SE/rNase A treated samples was used for subsequent tissue PRIME-PAINT.

Multiplexed imaging of pancreatic tumor sections with PRIME-PAINT

To exemplify multiplexed tissue SRM imaging, we chose to use FFPE sections of Pancreatic Ductal Adenocarcinoma (PDAC). Dual labeling for Tom20 and prognostic pan-cytokeratin could inform structural changes in detailed mitochondrial organization which are theorized to occur in PDAC development in tumor regions ~ 300 -500 μm wide or larger [25-28]. With PRIME-PAINT and sample optimizations described earlier, we were able to obtain high-quality, SRM images of both targets across an entire cancerous duct (**Fig. 6**).

A histological overview photographed with a 20x objective revealed a moderately differentiated PDAC within desmoplastic stroma (**Fig. 6A & B**). Using Cy3-labeled DS-conjugated antibodies as a reference, immunofluorescence imaging confirmed strong pan-cytokeratin signal along the duct and faint mitochondria both in and around the duct itself (**Fig. 6C**). By acquiring six FOVs with PRIME-PAINT at 0.3 mm x 0.3 mm single FOVs with 40 μm overlaps, we imaged the entire duct and adjacent stroma covering an area over 800 μm by 500 μm (**Fig. 6D**). At 30 minutes per FOV per target, the entire imaging took ~ 3 hours for each target and ~ 6 hours to obtain a dual-target image. A single FOV demonstrates the uniform image quality over the 0.3 mm x 0.3 mm area and highlights regions of the tumor with subtle differences in pan-cytokeratin expression (**Fig. 6E**). In smaller ROIs, subcellular details and morphology can be seen at unparalleled detail versus an otherwise diffraction limited blur (**Fig. 6F-H**). We note, not only can distinct mitochondria of varying size and shape be seen, but dense pan-cytokeratin also tapers to fine filamentous networks often enclosing the cell periphery and contained mitochondria. Finally, to further exemplify the full range of spatial information obtainable by PRIME-PAINT on FFPE tissue sections, we serially magnified a second ductal adenocarcinoma from the millimeter-scale of the histological overview down to distinct mitochondrial membrane structures (**Supplementary Fig. S13**).

Discussion

We have demonstrated PRIME-PAINT, a new platform for multiplexed imaging of cells and tissue sections across roughly five orders of length scales (~10 nm to mm scales). PRIME-PAINT is based on a simple optical design and capitalizes improvements in imaging kinetics, sample preparation, and programmable microfluidics. With PRIME-PAINT, multiplexed SRM imaging over mm² of sample areas could be achieved in as little as 40 minutes per target, significantly accelerating the use of SRM in addressing large cell populations and clinical samples.

By decoupling the illumination and detection paths, PRIME-PAINT afforded single FOVs up to ~0.5 mm x 0.5 mm, limited only by the size of the detector. In prior, through-objective configurations, the maximum FOV was optically capped at ~150-200 μ m [8-10] in spite of large-field capable hardware such as microscope frames and image sensors. The prism illumination scheme has already been used in numerous single-molecule imaging studies and should be readily adopted without needing sophisticated scanning schemes [9]. The ease of setting up and operating PRIME-PAINT does not compromise the effective spatial resolution, speed, nor the flexibility in switching targets at different depths. With PRIME-PAINT, we imaged membrane targets such as KRas and caveolae as well as cytosolic targets such as mitochondria and vimentin at 30-45 nm spatial resolution from hundreds of cells.

The integration of a microfluidic imaging chamber and buffer exchange system added multiple benefits and was an important, enabling component in PRIME-PAINT. Despite the slight complexity in working with the sandwiched sample chamber, the design has the advantage of being fully compatible with both tissue culture and standard FFPE section workflows. The sample chamber also allowed integration of programmable microfluidic capability to not only facilitate multiplexing but also high-quality tissue imaging via microfluidic-enhanced DNA-PAINT. The ability to refresh the imaging buffer via a mild flow when needed ensures consistency in imaging kinetics and image quality in long imaging sessions, for example when stitching multiple FOVs. These characteristics makes PRIME-PAINT ideally suited for full automation to image even larger areas on broad biological specimens.

Imaging at the throughput afforded by the PRIME-PAINT system raises new opportunities in combining experimental biology and computation. SRM already benefits from computational tools such as GPU-accelerated localizations [29-32], but recent work has also shown the promise of using SRM data to infer dynamic protein complexes [33, 34] similar to cryo-EM single-particle analysis (SPA) that has revolutionized structural biology. In this work, we utilized the open-source WEKA platform [18] to extract thousands to millions of nanostructures in PRIME-PAINT images followed with statistical analysis to infer changes in these structures across cell populations. The availability of large scale image data at the SRM scale synergizes well with the growing capacity in machine-learning and deep-learning based image analysis [33], which is predicted to significantly accelerate biomedical discovery [35, 36].

The ability to image FFPE sections at nanometer resolution across mm² FOVs is an important step toward clinical applications of SRM. Prior work using electron microscopy (EM) [37-39] and few recent studies using SRM [12, 13] have already demonstrated the importance of nanoscopic biological structures in normal tissue development and diseases like cancer, but they all were limited in throughput. We overcame obstacles that prevented high-quality DNA-PAINT on FFPE samples and achieved PRIME-PAINT on tissue sections with similar speed and image quality to those on cultured cells. Two-color PRIME-PAINT imaging revealed unprecedented details of mitochondria and pan-cytokeratin in PDAC samples (Fig. 7 and Fig. S8). To our knowledge, this is the first time that clinical samples have been analyzed with nanoscopic resolution with millimeter-scale FOVs. Hence, PRIME-PAINT joins the growing list of spatial omics tools [40-43] with the unique capability of analyzing nanoscopic protein localizations and interactions.

Lastly, PRIME-PAINT is permissive to further improvements to allow even higher imaging throughput, better spatial resolution, and 3D imaging. Through continued advances in imaging kinetics and image sensors, we expect the acquisition time to be even shorter than the current <1 hour per mm² per

target. We also expect the spatial resolution for PRIME-PAINT to increase to ~20 nm or better (currently 30-45 nm) simply by using a more powerful light source (currently ~1 W at 640 nm). Finally, the PRIME-PAINT system is amenable to automation through integration of the programmable fluidics, FOV stitching and buffer exchange[44], and on-line data processing [31, 45]. Leveraging recent progress in multiplexing strategies [46-48], 3D PRIME-PAINT imaging of tens of targets over >1 mm² sample areas should be feasible in the foreseeable future, ultimately enabling ‘Google-earth’ like view of biological systems.

Materials and Methods

Materials

Methods utilized for generating labeling reagents followed established protocols for DNA-PAINT-ERS [17]. In brief, all starting DNA oligonucleotides were obtained from Integrated DNA Technologies. Docking strands included a 5' amino modifier C6, for further conjugation with DBCO-PEG4-NHS (Click Chemistry Tools, A134-2) via succinimidyl ester chemistry, and a 3' Cy3TM fluorophore which helps confirm proper antibody labeling. Imaging strands with a 3' amino group were reacted using succinimidyl ester chemistry with NHS-ATTO 643 (ATTO-TEC, AD 643-31). All reactions were performed at room temperature in ultrapure water adjusted to pH~8.5 using 1 M sodium bicarbonate (Fisher Scientific, M-14636) for 3 h. Conjugated DNA oligos were purified via ethanol precipitation, and resuspended in InvitrogenTM UltraPureTM DNase/RNase-Free Distilled water (Thermo Fisher Scientific, 10977023).

Secondary antibodies used were: AffiniPure Donkey anti-Rabbit IgG (H+L) (Jackson Immuno Research 711-005-152), AffiniPure Donkey anti-Mouse IgG (H+L) (Jackson Immuno Research 715-005-150) and AffiniPure Donkey anti-Chicken IgG (H+L) (Jackson Immuno Research 703-005-155); these were conjugated with azido-PEG4-NHS via succinimidyl ester chemistry. Antibody-PEG4-azide conjugates were purified through a 50 kDa Millipore SigmaTM AmiconTM Ultra Centrifugal Filter Unit (Fisher Scientific, UFC505096). Next, purified antibody-PEG4-azide were reacted with excess DBCO-DS (molar ratio 1: 5) via copper-free click chemistry, overnight at room temperature using a rocker. Antibody-DS products were isolated through a 100 kDa Millipore SigmaTM AmiconTM Ultra Centrifugal Filter Unit (Fisher Scientific, UFC510096). Protein concentrations and the degrees of labeling were found using the peak signals at 260, 280 nm, 550 nm (for Cy3TM) in a Nanodrop UV-Vis spectrophotometer (ThermoFisher Scientific, 2000c). In general, oligo-conjugated secondary antibodies generated contained 4-5 conjugated DS oligos.

The SNAP-tag substrate BG-PEG4-Azide was synthesized by the Medicinal Chemistry Core at Oregon Health and Science University. Briefly, it was synthesized in two steps via an amine-reactive key intermediate prepared from commercially available BG-NH₂ as the starting material, followed by an NHS-ester crosslinking reaction. The final crude product was purified by preparative HPLC. The structure and purity of BG-PEG4-Azide were further confirmed by analytical HPLC analysis and high-resolution mass spectrometry prior to the click oligonucleotide labeling. BG-PEG4-Azide was reacted with excess DBCO-DS (molar ratio 1:10) via copper free click chemistry, on a rocker at room temperature overnight. The resulting BG-DS was purified via ethanol precipitation, and suspended in UltraPureTM DNase/RNase-Free Distilled water. The concentration was determined by the Nanodrop UV-Vis spectrophotometer, similarly as mentioned above.

Primary antibodies used were: Mouse-beta tubulin monoclonal antibody (Thermo Fisher Scientific, 32-2600), Rabbit-anti-Tom20 polyclonal antibody (Abcam, ab78547), Rabbit-anti-caveolin-1 antibody (Abcam, ab2910), Chicken-anti-vimentin antibody (Sigma Aldrich, AB5733), and Mouse panCytokeratin (Abcam, ab7753).

For all remaining experimental steps and sample processing and labeling (Fixation, permeabilization, and immunostaining, etc) materials used included: paraformaldehyde (Sigma-Aldrich, P6148), Triton X-100 (Sigma-Aldrich, X100), 25% glutaraldehyde (Sigma-Aldrich, G6257), bovine serum albumin (Fisher Scientific, BP1600), sodium hydroxide (Fisher Scientific, S318-100), sodium borohydride (Sigma-Aldrich, 452882), Invitrogen™ Salmon Sperm DNA (Thermo Fisher Scientific, AM9680), sodium azide (Fisher Scientific, AC190381000), Gibco™ Dulbeccos PBS with calcium and magnesium (PBS+) (Thermo Fisher Scientific, 14-040-182), and 50 nm gold particles (BBI Solutions, EM.GC50/4). Fixation was performed using a buffer made from: 2x PHEM buffer, generated with 0.06 M PIPES (Sigma-Aldrich, P6757), 0.025 M HEPES (Fisher Scientific, BP310-500), 0.01 M EGTA (Thermo Fisher Scientific, O2783-100), and 0.008 M MgSO₄ (Acros, 4138-5000) in distilled water, 10 M potassium hydroxide (Sigma-Aldrich, 221473) was used to finally adjust the pH to 7. As with DNA-PAINT-ERS, a % volume combination of EC (Sigma-Aldrich, 676802) with buffer C (PBS plus 500 mM Sodium Chloride) was used as indicated for both imaging and even washing steps.

Flow-chamber preparation and cell culture

Flow chamber substrates were made using: 25x75mm fire-polished microscope slides (Schott, Nexterion® Slide Glass B 1025087). Fire-polished microscope slides were each drilled twice using a 1/16th inch bit diamond coated drill bit (Lasco Diamond #F6) for later use as microfluidic inlet and outlet ports, at the coordinates of (4 mm, 16 mm)- and (21 mm, 59 mm) on the 25x75mm coverslide. After drilling, slides were rinsed with DI water (3x), and sonicated in 100 % EtOH for 10 minutes. Following 3x DI water rinses, slides were etched in 1M NaOH for 20 minutes. After three rinses with DI water, cleaned slides were left in 100% EtOH prior to cell culture/tissue slide preparation.

Cell and Tissue samples

Cell lines used in this study included U2OS (ATCC®, HTB-96) and COS7 (ATCC® CRL-1651™). U2OS and Cos7 cells were passaged every 3–4 and 2–3 days respectively, and cultured in Gibco DMEM (Thermo Fisher Scientific, 11995073) mixed with 10% fetal bovine serum (Thermo Fisher Scientific, 26-140-079). Passaging was performed using Trypsin-EDTA (0.25%) (Thermo Fisher Scientific 25200056), with cells kept to below 15 passages. For SRM imaging experiments, cells were grown on custom drilled coverslides within a sterile oval silicon cutout until 50-60% confluency prior to fixation.

All patient FFPE tissue samples (including HER2+ breast cancer and PDAC samples) were collected through either the OHSU Biorepository or the Brenden Colson Center following IRB approved protocols including patient consent for research applications. Standard human pancreas samples obtained by BCC were FFPE sections from otherwise healthy cadavers and were used for most tissue imaging optimizations. FFPE tissue samples were cut using a ultramicrotome in 2 μm thick sections (RM2125 RTS, Leica Biosystems, Germany).

Pre-drilled and cleaned fire-polished coverslides were prepared for tissue mounting using Poly-Ethylene-Imine (PEI) (Sigma--Aldrich, 904759-100G) coating. In brief, cleaned coverslides were treated for 20 minutes with 0.1% PEI solution in ultrapure H₂O. After coating, excess PEI was rinsed 3x with ultrapure H₂O for 5 minutes each. After aspirating excess H₂O, coated slides were left to dry flat at 42°C for 2+ hrs, or until completely dried. Fluidic chamber profile outlines were drawn onto the non-PEI-coated backside using a ultrafine sharpie to assist in tissue mounting positioning. All tissue samples were sectioned at 2μm ±0.5μm thickness, floated on a 42°C waterbath immediately prior to mounting onto PEI-coated coverslides. Mounted tissues sections were dried vertically for 1 hour at 60°C before storage. Mounted tissue sections were stored vertically in this manner for up to 1 month prior to antigen-retrieval, labeling and imaging.

Immunostaining

For immunostaining of caveolin and SNAP, cells were fixed for 20 min with 3.7% paraformaldehyde (PFA) in 1x PHEM buffer, after a quick PBS wash. Following two PBS washes, cells were quenched with fresh 0.1% sodium borohydride in PBS for 7 min, and followed 3 washes with PBS (5min each). Cells were permeabilized with 0.3% saponin in PBS for 20 min. For immunostaining of microtubules, Tom20 and vimentin, cells were fixed for 20 min with 3.7% PFA and 0.1% glutaraldehyde (GA) in 1x PHEM, followed by 3x PBS washes, quenching with sodium borohydride and permeabilization in 0.2% Triton X-100 in PBS. Blocking in PBS with 3% bovine serum albumin, 5% salmon sperm DNA (Thermo Fisher Scientific, AM9680) for 45 min was done on a rocker, followed by incubation with the primary antibody for Tom20 (1:250), caveolin (1:200), tubulin (1:100) or vimentin (1:250) antibodies in PBS buffer containing 3% BSA. The incubation took place overnight on a rocker at 4°C in a humidity chamber. Next, cells were washed three times (5 min each) with PBS before incubation with respective secondary antibody-DS described above at a final concentration of $\sim 8 \mu\text{g mL}^{-1}$ in PBS buffer containing 1% BSA and 5% salmon sperm DNA; the secondary antibody incubation also took place on a rocker at room temperature for 90 min. For DS secondary antibody incubation and subsequent steps, the sample was kept in the dark to avoid bleaching of conjugated fluorophores. Cells were washed three times with PBS (5 min each). All cell samples were post-fixed for 10 min with 3.7% PFA and 0.1% GA in 1x PHEM. Before imaging, cells were incubated with 15% 50 nm gold particles in PBS+ for 1 min, followed by a quick PBS wash.

For immunostaining of FFPE tissue samples, FFPE sections were deparaffinized using xylene (2x, 10 min), 100% EtOH (2x, 10 min) 95% EtOH in DI water (5 min), 70% EtOH in DI water (5 min), 50% EtOH in DI water (5 min) and left in PBS. Tissues underwent antigen retrieval in a decloaking chamber (Bio SB, BSB-7087) first in Tris buffer (300mM Tris, 0.05% Tween 20, PH 8). Tissues were transferred into a pre-heated citrate buffer (300mM NaCitrate Monohydrate, 0.05% Tween 20, PH 6), also heated during decloaking, and allowed to cool to room temperature. After two PBS washes, tissues were further permeabilized with 0.4% Triton X-100 in PBS for 45 minutes. After removing excess permeabilization solution and three PBS washes, a hydrophobic barrier (company product) was applied around the mounted tissue following the fluidic outline of the chamber design. Tissues were either further treated with RNaseA/ Image-iT® FX signal enhancer (ThermoFisher Scientific, I36933) or directly blocked prior to antibody labelling. In brief, RNase A and signal enhancer treatment both occurred prior to antibody labeling as optional optimizations. After permeabilization, tissue samples could be treated with RNase A (ThermoFisher Scientific, EN0531) at 50x dilution in PBS on a rocker for overnight at room temperature. After a rinse with PBS, sections were quenched with fresh 0.1% sodium borohydride in PBS for 7 min, and followed by three washes with PBS (5min / each). Tissue was further incubated with signal enhancer at room temperature for 30 minutes, followed by three washes with PBS wash (5 min/each).

After PBS washes, tissues were blocked with 3% BSA and 0.3% saponin in PBS for 1 hour. Next, tissues were incubated with primary antibodies: Tom20 (1:200 dilution), and panCytokeratin (1:150 dilution) in PBS containing 3% BSA and 5% salmon sperm DNA. The incubation took place on a rocker overnight at 4°C in a humidity chamber. Following three PBS washes (5 min each), tissues were incubated with respective DS-conjugated secondary antibodies at a final concentration of $\sim 8 \mu\text{g mL}^{-1}$ in PBS buffer containing 1% BSA and 5% salmon sperm DNA. The incubation also took place on a rocker at room temperature for 2 hours, followed by three PBS washes (5 min each). After which, all tissue samples were post-fixed by 3.7% PFA and 0.1% GA in 1x PHEM at room temperature for 30 min. Before flow chamber assembly, tissues were incubated with 15% 50 nm gold particles in PBS+ for 1 min, followed by a quick PBS wash.

Flow Chamber assembly

Flow chamber exterior was made using a CNC-cut aluminum holder which fits gently outside the sample sandwich, providing compression to meet matching 1/16 fractional width O-rings (McMaster-

Carr, 2418T11) and Tygon tubing (Cole-Parmer, EW-06419-01) at the pre-drilled points on the coverslide. This external holder and microfluidic tubing can be easily reused for each sample (see .CAD file, Supplementary software). Since the sample coverslide still provides the backbone of the fully assembled sample and fluidics for imaging, both the microscope objective and prism can be used at nearly identical positions between samples.

To complete flow chamber interior assembly around immunolabeled cells/tissues mounted to pre-drilled coverslides, 24 mm x 40 mm high-precision #1.5 coverslips (Thorlabs, CG15KH), and 2-inch wide Behm's® Parafilm (Thermo Fisher, 12-374-16) were first combined. After sonicating coverslips in 100 % EtOH for 10 minutes, coverslips were quickly air dried using a gentle stream of compressed air. Parafilm was cut into 1 inch wide sections and stretched length-wise until just prior to tearing. Stretched Parafilm was placed onto coverslips such that no folds or air-pockets were present. Excess Parafilm was removed from the coverslip border using a razorblade, and fluid profile stencil was used to cut the flow chamber interior into the parafilm. After peeling the inner part of the Parafilm, the coverslip and fluidic profile were ready for final assembly. After removing excess PBS from cells/tissues, coverslips with fluidic profiles were slowly placed on top of the coverslide with sample such that no excess solution contacted the Parafilm border. A 110 W glue gun tip (with glue removed) was used to gently press the coverslip along the Parafilm border to melt the Parafilm and seal the fluidic chamber.

Fluidic components used were MX Series II™ 10 Position/11 Port Selector Valve (IDEX Health & Science, MXX778-605) and RP-TX Peristaltic Pump (Takasago Electric, RP-TXP5S-P04A-DC3VS). Pump control was achieved through Arduino Uno (Amazon, X7375-10G) and Adafruit Motor/Stepper/Servo Shield for Arduino v2 Kit (Adafruit, 8541582581). Both the port selector and peristaltic pump were controlled via custom C code (see Supplementary software).

Microscopy

Through-objective TIRF superresolution data in this work were taken on a custom single-molecule imaging system described previously [17]. Briefly, two lasers emitting at 561 nm (Opto Engine LLC, 150 mW), and 647 nm (Coherent OBIS 647, 140 mW) were combined and introduced into the back of a Nikon Ti-U microscope equipped with a 60× TIRF objective (Nikon, Oil immersion, NA 1.49). An $f = 400$ mm lens was placed at the back port of the microscope to focus the collimated laser light to the back aperture of the objective to achieve objective TIR illumination. The excitation light can be continuously tuned between epi-fluorescence and strict TIR angle modes by shifting the incident laser horizontally with a translational stage before entering the back port of the microscope. Additionally, a weak cylindrical lens compensates for longitudinal beam widening through the prism, to maintain power density over a round FOV for efficient single-molecule excitation. A custom focus stabilizing system based on detection of the reflected excitation laser was used to stabilize the focus during data acquisition. A multi-edge polychroic mirror (Semrock, Di01-R405/488/561/635) was used to reflect the lasers into the objective and clean up fluorescence signals from the sample. Emission filters used for the 561 nm (for imaging Cy3 on the DS), and 647 nm (for imaging ATTO643 conjugated ISs) were FF01-605/64 and FF01-708/75, respectively (all from Semrock). Fluorescence signals were collected through the objective by an electron-multiplied charge-coupled device (EM-CCD, Andor, iXon Ultra 897) using a typical EM gain setting at 200–300 in frame transfer mode. Unless otherwise indicated, the power density of the 647 nm laser (for DNA-PAINT imaging using ATTO643 conjugated IS) was typically around ~ 500 W/cm².

Prism-type TIRF PRIME-PAINT data was collected using a custom single-molecule imaging system as outlined in Fig. 1A. Key system components used from the laser to the camera were: 1W 639 nm laser (Opto Engine, MRL-FN-639-1W), 2x beam expander (ThorLabs BE02M-A), cylindrical lens $f=1000$ mm, 5x beam expander (ThorLabs GBE05-A), 2-5x continuous beam expander (ThorLabs BE02-05-A), 4π lens cage (using an $f = 100$ mm and an $f = 80$ mm lens), 10 mm Square Aperture UV Fused Silica Prism (Pellin Broca, ADBU-10), 40x silicon oil objective (Nikon, Plan APO 40x/1.25 Sil λ S WD 0.3, MRD73400), 647nm long pass filter (Semrock, LP02-647RU-50), 633 nm Stopline® notch filter

(Semrock NFD01-633-25x36), and finally either a side-mounted Prime-95B sCMOS (Teledyne Photometrics, Prime 95B 25MM) or Kinetix sCMOS (Teledyne Photometrics). All detection path components housed within a Nikon Eclipse Ti2-E microscope body. Perfect Focus Unit (Nikon PFS, TI2-N-NDA-P) was integrated into the microscope body and provided stable autofocusing even during mild flow integration during PRIME-PAINT imaging.

Data acquisition and image processing

Superresolution images were acquired using the open source micromanager software suite (<https://micro-manager.org/>)[49] and saved as OMERO TIF files. Image analyses for extracting single-molecule localization and subsequent localization filtering, sorting, and rendering was performed using in-house Matlab scripts[50]. Briefly, raw localizations were first filtered based on localization fitting parameters such as signal to noise ratio, widths of point spread functions in the x and y dimensions, aspect ratio, etc. Next, the localizations were sorted, during which events that appeared within a defined number of frames (typically 2–3) and distance (typically 80 nm) were then combined into a single event with averaged coordinates. The sorted localizations were then used for final image rendering, and the rendered images were saved as TIF files for further analysis and annotations in Fiji. Multi-color images were co-registered using an average of observed gold fiducial positions within each FOV, while multi-FOV stitched images were aligned using average position of observed overlapping gold fiducials along shared image boundaries.

Custom Machine-learning integrated Fiji Macro

Our analysis Macro was built using the Fiji macro language in .ijm format, and can be found here (Supplementary software). Machine learning segmentation/classification was performed using Trainable WEKA Segmentation plugin within Fiji [18]. Training was performed using input images with manually drawn caveolae particle boundaries trained against background diffuse cytoplasmic caveolin-1. Subsequent testing of trained model performance against manually annotated caveolae on three additional datasets resulted in a DICE coefficient of $84\% \pm 8\%$.

Macro workflow is visually shown in Supplementary Fig. S5. This begins by opening a multi-target PRIME-PAINT rendered image, typically 29,100 x 29,100 pixels, and using Fiji ROI manager to manually draw boundaries for each cell of interest to quantify. After initiation, the full PRIME-PAINT image is loaded into the WEKA plugin and the trained .model file for caveolae is loaded, with all subsequent steps happening automatically. For each picked cell ROI, the macro will cut the cell out of the full PRIME-PAINT image, masking signal outside the ROI, and automatically generate sub-images with an adjustable overlap to tile across each cell ROI analyzed. Each sub-image is temporarily saved, and WEKA classification is performed on each cell's sub-image. After classifying each sub-image of a particular cell, dynamic offsets initially added during sub-image generation are removed and the full classified cell is combined using original coordinates. Distinct ROI for all detected vesicles are saved and used to measure original cell image attributes at the positions indicated from WEKA classification outputs. In practice, our custom Fiji macro would automatically segment caveolae from input cells at a rate of ~30 minutes per cell, although this performance will vary depending on the computer specifications used. These per-cell caveolae measurements are saved as .csv outputs and can be post-processed using programs such as R.

Population analysis and other plots

Outside of rendered images, all plots were generated in R using the ggplot package. Caveolae particles smaller than 20 nm were excluded from downstream analysis as their border could not be reliably determined and were not considered as a part of initial manual annotation for observed caveolae particles. Population analysis was performed using the nls() function in R, which was used to model a two gaussian population within the total observed populations of caveolae particle sizes according to diameter.

Statistical analysis

Image analysis was performed using custom semi-automated machine learning macro installed in ImageJ (see Supplementary Fig. S5 & Supplementary software). DNA-PAINT images with manually annotated cell boundary .roi were input to extract caveolae particle positions as .roi lists. Mapping these per-caveolae particle .roi positions onto the original image, the ImageJ “Measure” function was used to extract and save .csv files per cell, with image attributes including Area, Diameter, Mean intensity, etc. All downstream analysis and visualization was performed in R. P-value calculations in Fig. 5B were performed using the Wilcoxon test in the `stat_compare_means()` function within the `ggplot` package in R. For Fig. 5C, the Y axis of size population prevalence calculated using the `geom_density` function in `ggplot` from \log_{10} -transformed X axis of all caveolae particle diameters.

Acknowledgments

The authors thank Drs. Joe W Gray, Gordon Mills, Terry K Morgan, Young Hwan Chang, Jason Link, Sean Speese, Yu-Jui (Roger) Chiu, David Qian, and many other colleagues at OHSU for their helpful discussions. M.J.R, F.C., J.K., D.H., T.Z., S.E., and X.N. are members of and supported by the Cancer Early Detection Advanced Research (CEDAR) Center of the OHSU Knight Cancer Institute. Research in the Nan lab is supported by the OHSU Knight Cancer Institute, the Damon Runyon Cancer Research Foundation, the Cancer Systems Biology Consortium from the National Cancer Institute (CSBC, grant number U54 CA209988, PI: Joe W. Gray), and the National Institute of General Medical Sciences (grant number R01 GM132322, PI: X.N.).

Supplementary materials

Please see attached Supplemental information (.pdf containing supplementary figures S1-12) and Supplementary software (.zip file containing programs and scripts used for hardware control and analysis).

Author contributions

Conceptualization: XN, FC, MR; Methodology: MR, XN, JK, DH, KT, TZ, MS, JS; Investigation: MR, JK, DH, KT, TZ; Visualization: MR, JK; Supervision: XN, SE; Writing—original draft: MR, XN; Writing—review & editing: MR, XN, MS, KT, TZ, SE

Competing interest

All other authors declare they have no competing interests.

Figures and Tables

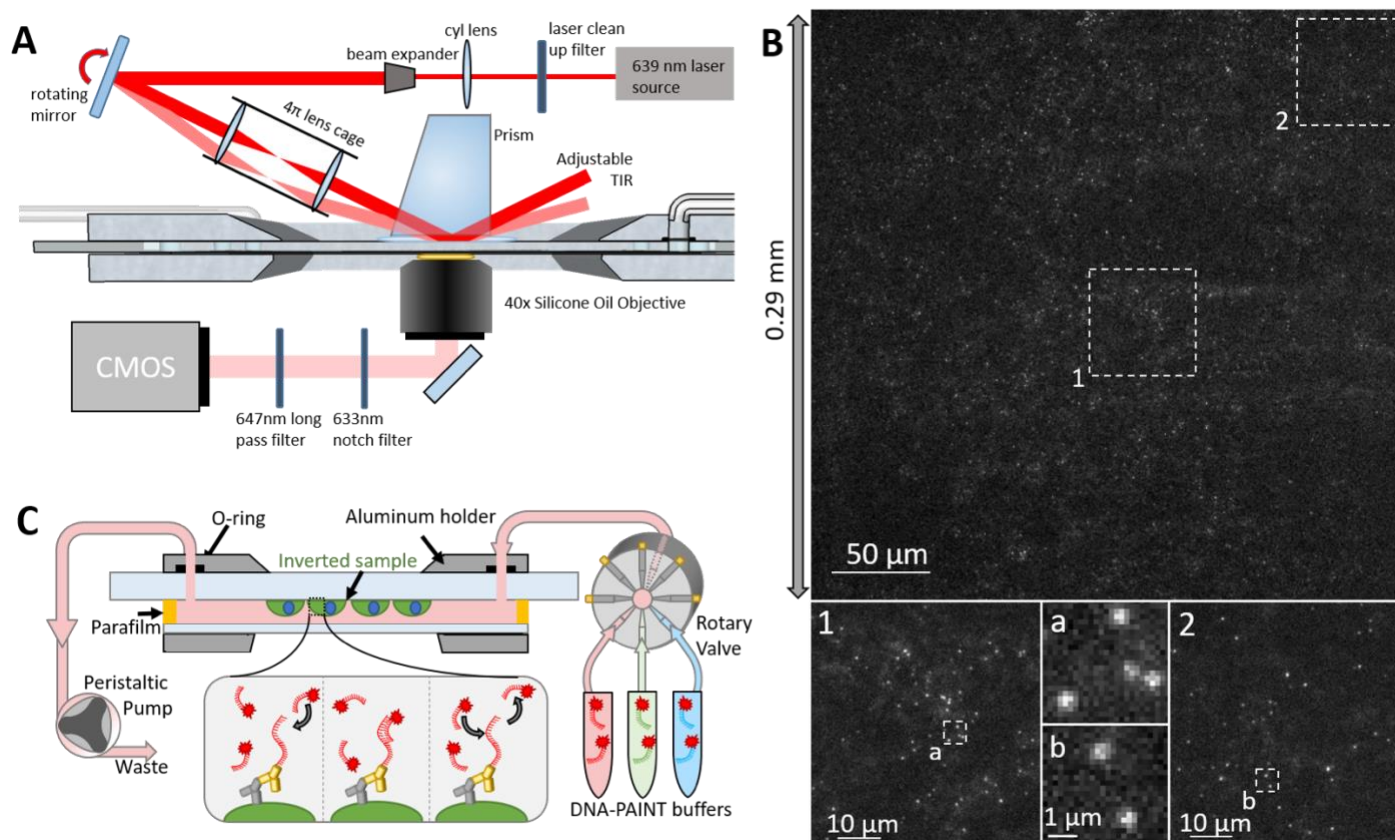


Fig. 1: Overview of PRIME-PAINt optics, fluidics, and example SMLM images

(A) Schematic of the PRIME-PAINt microscope design and general imaging strategy, with the widened laser beam and controllable TIR angle; (B) Representative PRIME-PAINt raw image at 30 ms exposure highlights single-molecule localization quality. Single-molecule events are clearly resolved both in the center on the FOV, and near the corners, exemplifying the 300 μm x 300 μm FOV; (C) Schematic cross-section of the flow chamber assembly and sample position. Notably, cultured cells/mounted tissue are attached on an inverted sample coverslide, enabling both encapsulation of imaging solutions and buffer exchange for multi-target DNA-PAINT imaging. DNA-PAINT imaging utilizes oligonucleotide-conjugated antibodies (DNA in red, antibody in yellow) and complimentary imaging strand (IS, also shown in red with a fluorophore represented by a red star) to provide transient single-molecule localizations while freely diffusing strands contribute only slightly to background fluorescence.

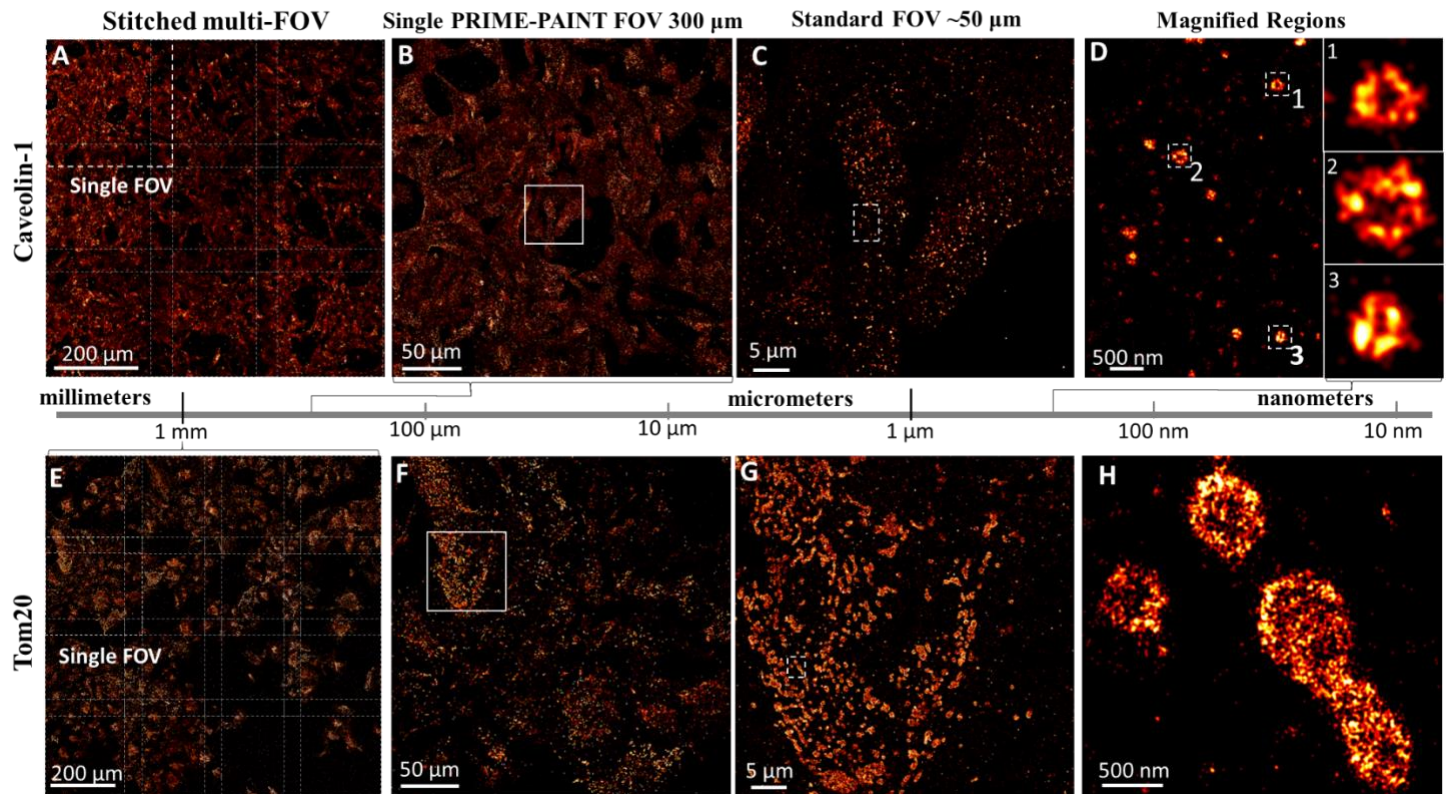


Fig. 2: PRIME-PAINT imaging of caveolae and mitochondria over millimeter FOVs in U2OS cells.

Representative single and stitched PRIME-PAINT images of membrane-adjacent caveolae (**A-D**) and cytosolic Tom20 (**E-H**). (**A**) Stitched 3x3 array of membrane-adjacent caveolae at 800 μm x 800 μm FOV with 40 μm overlaps. (**B**) Single PRIME-PAINT FOV at nearly 300 μm x 300 μm of Caveolin-1 imaged with strict TIR angle. (**C**) Magnified region from **B** highlighting the detail within a more standard smaller FOV of ~50 μm . (**D**) Magnified cell region from **C** and 3 insets showing high-quality super-resolution detail of caveolae vesicles. (**E**) Stitched 4x4 array of cytosolic Tom20 over 1 square millimeter. (**F**) Single PRIME-PAINT FOV at nearly 300 μm x 300 μm . (**G**) Magnified region from **F** highlighting mitochondria within a more standard smaller FOV of ~50 μm . (**H**) Magnified cell region from (**G**) with distinct mitochondria. Each single PRIME-PAINT image (**B,F**) was acquired in 15 minutes (30,000 frames at 30ms exposure) using 1 nM IS2-ATTO643 and 12.5% EC for both Caveolin-1 and Tom20. Stitched 3x3 FOV for caveolae was acquired in 135 minutes while 4x4 FOV for Tom20 was acquired in 240 minutes. Scale bars are 200 μm in (**A,E**), 50 μm in (**B,F**), 5 μm in (**C,G**), and 500 nm in (**D,H**). Insets in (**D**) are 300 nm wide.

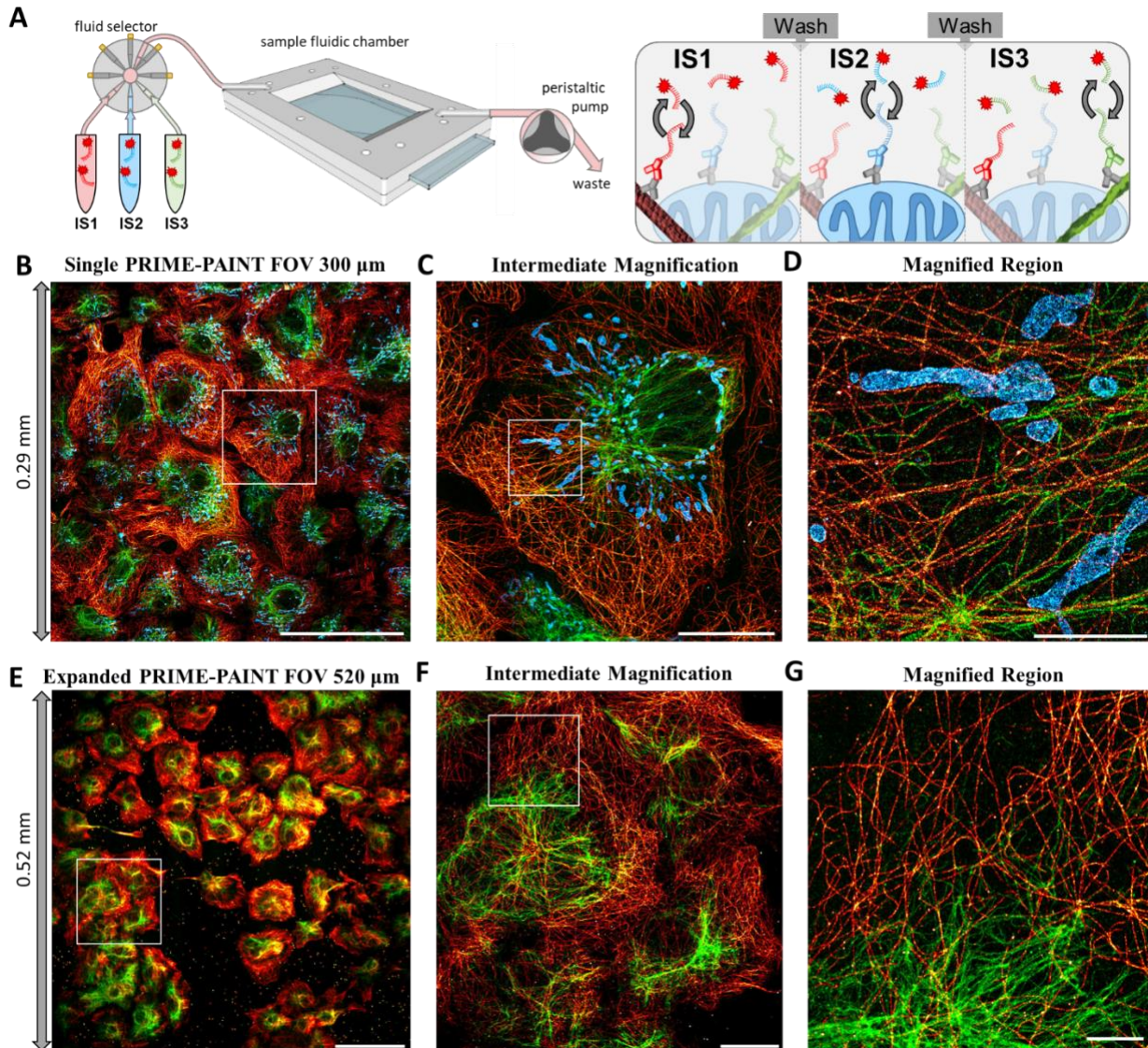


Fig. 3: Multiplexed PRIME-PAINT images using microfluidic exchange-PAINT.

(A) Schematic of multiplexed imaging with complimentary imaging strand (IS) targeting docking strand (DS) to microtubules (red), mitochondria (blue), and vimentin (green). (B) Single PRIME-PAINT 3-target image of Cos7 cells at 300 μm x 300 μm . (C) Magnified region from **B** highlighting image quality over a more standard ~ 50 μm FOV. (D) Magnified region from **C** showing distinct cytoskeletal structures and mitochondria. (E) Expanded PRIME-PAINT 2-target FOV at 521 μm x 521 μm . (F) Intermediate magnification from **E** at 100 μm FOV. (G) Magnified region from **F** highlighting dense perinuclear vimentin and extended microtubule networks. The representative 3-target image (**B-D**) was acquired in 45 minutes total (30,000 frames at 30ms exposure for each target) using 1 nM IS1-ATTO643 and 12.5 % EC, 1 nM IS2-ATTO643 and 12.5 % EC, and 500 pM IS3-ATTO643 and 13.75 % EC for microtubules, mitochondria, and vimentin respectively. Expanded PRIME-PAINT FOV 2-target image (**E-G**) was acquired in 30 minutes total (30,000 frames at 30ms exposure for each target) using 1 nM IS1-ATTO643 and 12.5 % EC, and 500 pM IS3-ATTO643 and 13.75 % EC for microtubules and vimentin respectively. Scale Bars are 100 μm in (**B,E**), 20 μm in (**C,F**), and 5 μm in (**D,G**).

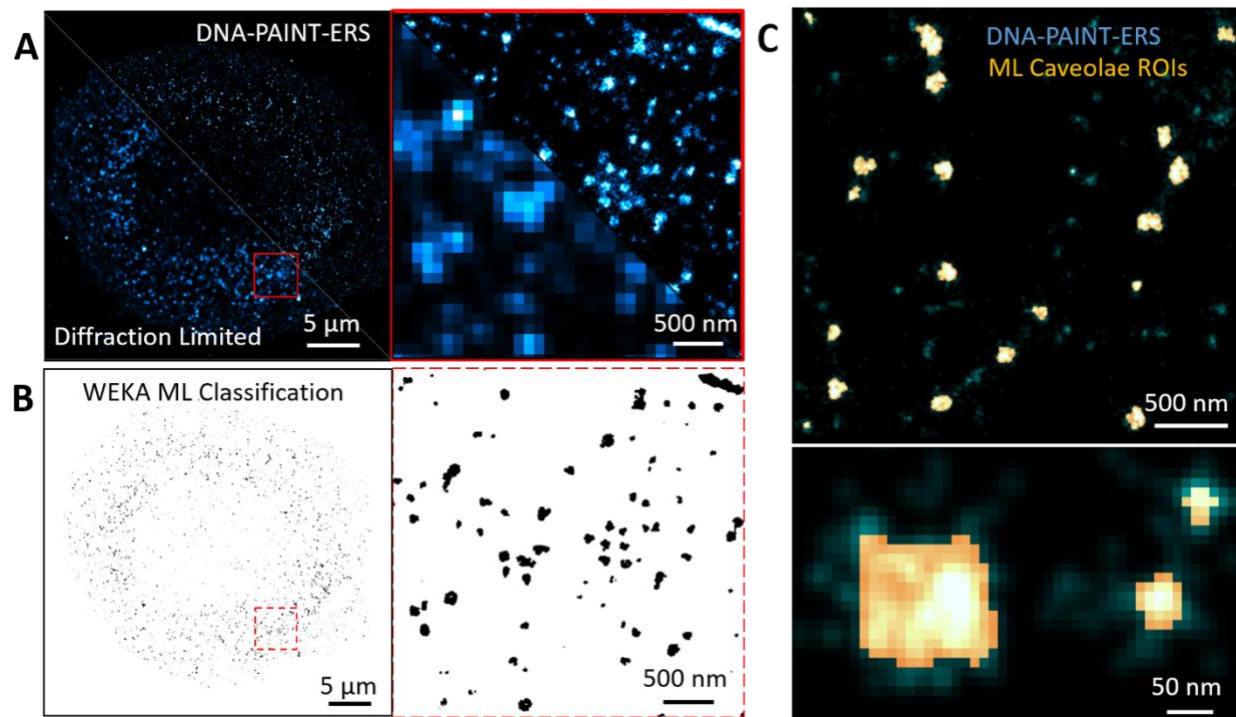


Fig. 4: PRIME-PAINT machine-learning segmentation and quantification of diffraction-limited structures.

(A) Representative image of Caveolin-1 within a single U2OS cell from an PRIME-PAINT image, diffraction limited view shown via diagonal split (left). Magnified region from solid red square where notably a diffraction limited resolution (200 nm resolution and 100 nm pixel size) is insufficient to see distinct caveolae vesicles (right). (B) Machine learning based image segmentation for caveolae vesicles using the input cell from A, as analyzed by custom Fiji-macro utilizing open-source WEKA classification (left). Magnified region from dotted red square showing caveolae outlines identified in A (right). (C) Representative overlays showing both caveolae vesicles as imaged via PRIME-PAINT in blue with corresponding caveolae outlines identified via machine learning segmentation in yellow (top). Inset showing both larger caveolae plaques and punctate caveolae vesicles, at ~150 nm and ~60 nm wide, respectively (bottom). Workflow for custom Fiji macro is shown in Supplementary Fig. S5.

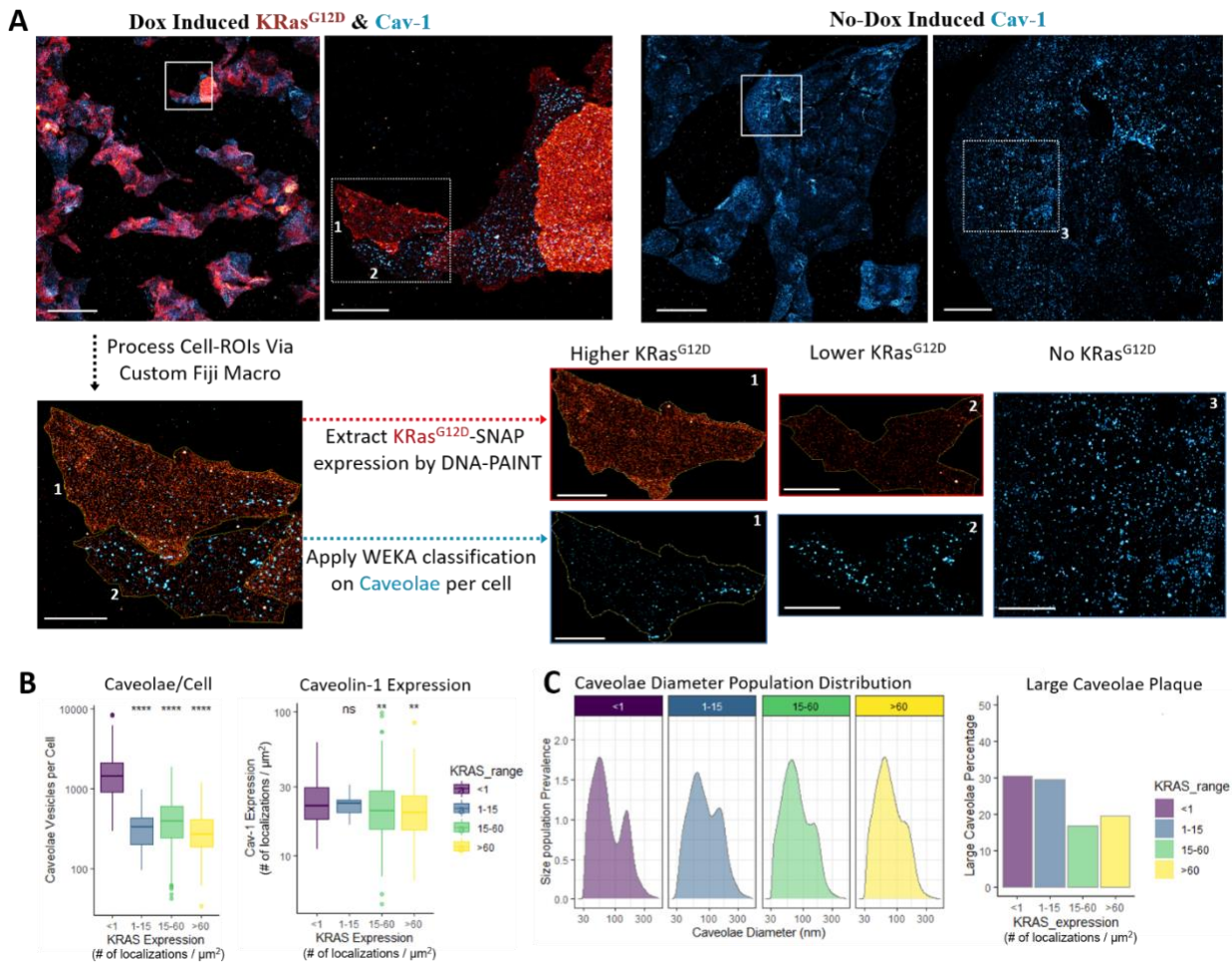


Fig. 5: Proof of principle PRIME-PAINT image analysis of the effect of KRas G12D overexpression on caveolae formation.

(A) Representative PRIME-PAINT images of both dox-induced and non-dox induced KRas G12D and Caveolin-1. KRas G12D labeled via SNAP-tag DS-1 conjugate shown in red, with Caveolin-1 DS2 shown in blue. Magnified regions show representative cells numbered 1,2, and 3 with higher, lower, and no KRas G12D expressions respectively. Manually annotated cell boundaries were subsequently input into custom Fiji macro for both KRas G12D expression and WEKA classification of caveolae vesicles per cell. (B) Boxplot of the abundance of quantified caveolae vesicles versus ranges of mutant KRas expression (in units of # of localizations per μm^2) for non-dox (<1), 1-15, 15-60, and >60 mutant KRas/ μm^2 . Boxplot of total Caveolin-1 expression versus ranges of mutant KRas expression per cell, with both expression values shown in # of localizations per μm^2 . (C) Population analysis of caveolae diameters for indicated KRas expression ranges, notably showing two main peaks at ~60 nm and ~150 nm from non-dox induction. Y-axis is the relative population of caveolae at differing diameters on the X-axis (log₁₀ scaled). Higher KRas G12D expression anti-correlates with the larger caveolae size population. Analysis was performed on 10 images of dox-induced and two images of non-dox induced cells acquired with 30,000 frames at 30 ms exposure for each target, using 1 nM IS1-ATTO643 and 12.5 % EC, and 500 pM IS2-ATTO643 and 13.75 % EC for KRas G12D-SNAP-DS1 and Caveolin-1-DS2 respectively. Scale bars in (A) are 50 μm for full FOV images (left for each cell condition), 10 μm for matching magnified views (right), and 5 μm for all example cells (bottom panels). Plots in (B,C) were generated using ggplot package in R. Significance levels (in panel B) were calculated using wilcox test from average values within each cell relative to the non-dox induced cells group.

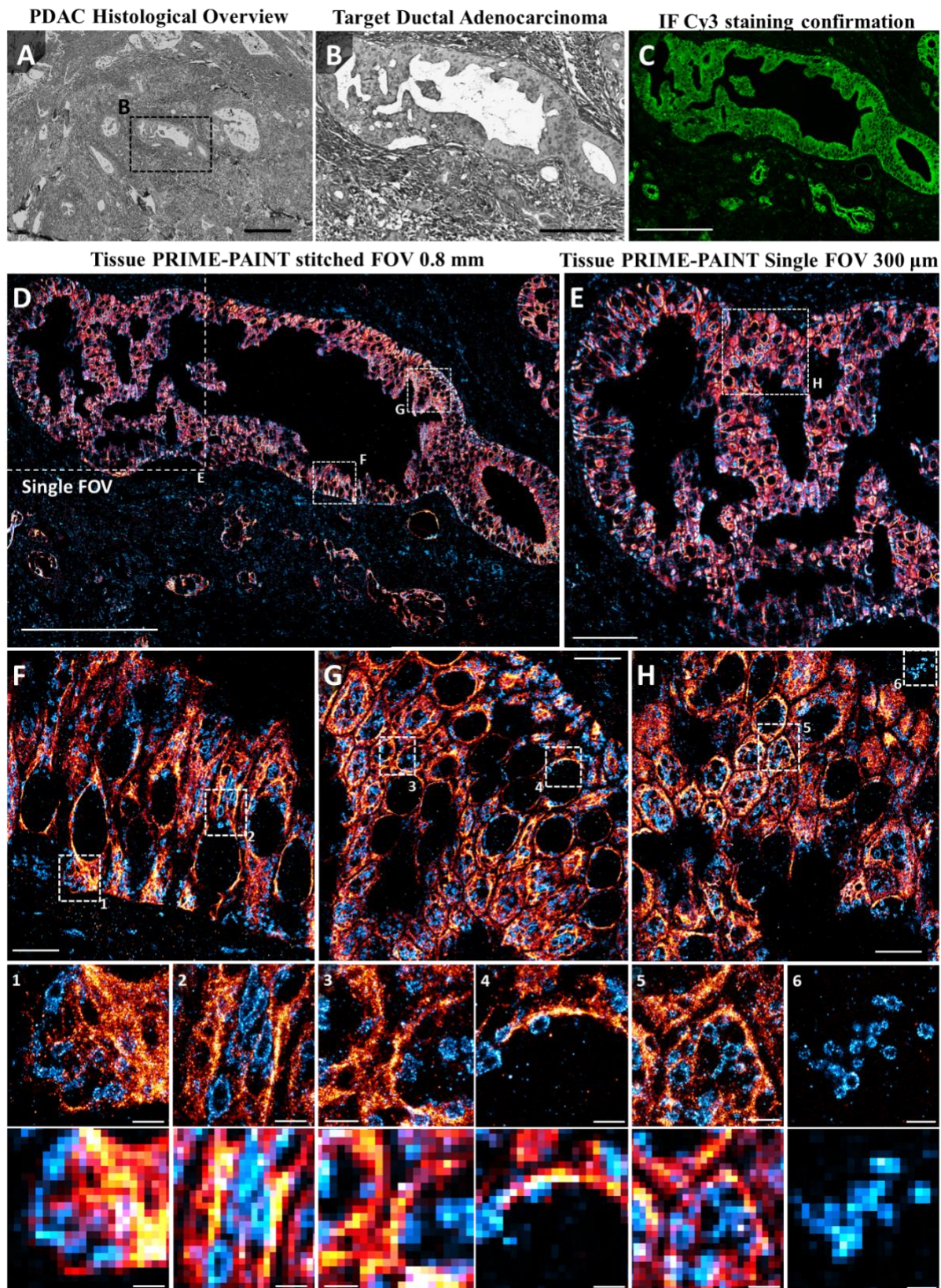


Fig. 6: Multiplexed PRIME-PAINT of pancreatic cancer tissue.

(A) Histological overview of moderately differentiated PDAC within desmoplastic stroma acquired at 20x magnification. (B) Targeted ductal adenocarcinoma for imaging with PRIME-PAINT. (C) Immunofluorescent confirmation of Cy3 signal from secondary antibodies conjugated to docking strand oligos showing strong pan-cytokeratin staining along the tumor and diffuse mitochondrial labeling within the tumor and adjacent stroma. (D) Stitched tissue PRIME-PAINT image of an entire, 800 μm long ductal adenocarcinoma with both prognostic pan-cytokeratin in red and mitochondrial Tom20 in blue. (E) Single tissue PRIME-PAINT image obtained under mild flow ('microfluidics-enhanced'). (F-H) Select magnified regions from (D,E) highlighting the high quality imaging of cellular features seen within different regions of the tumor. Numbered insets shown with matching diffraction limited views (300 nm pixel size). Tissue PRIME-PAINT 2-target images (E-G) were acquired in 6 hours total (30,000 frames at 60 ms exposure for each target) using PRIME-PAINT at 1 $\mu\text{L}/\text{min}$ flow and 500 pM IS1-ATTO643 and 7 % EC, and 500 pM IS2-ATTO643 and 7 % EC for pan-cytokeratin and Tom20 respectively. Scale bars are 500 μm in (A), 200 μm in (B-D), 50 μm in (E), 10 μm in (F-H), and 2 μm for both PRIME-PAINT and diffraction-limited bottom numbered insets.

References

1. Betzig, E., et al., *Imaging intracellular fluorescent proteins at nanometer resolution*. *Science*, 2006. **313**(5793): p. 1642-5.
2. Hess, S.T., T.P. Girirajan, and M.D. Mason, *Ultra-high resolution imaging by fluorescence photoactivation localization microscopy*. *Biophys J*, 2006. **91**(11): p. 4258-72.
3. Rust, M.J., M. Bates, and X. Zhuang, *Sub-diffraction-limit imaging by stochastic optical reconstruction microscopy (STORM)*. *Nat Methods*, 2006. **3**(10): p. 793-5.
4. Schnitzbauer, J., et al., *Super-resolution microscopy with DNA-PAINT*. *Nat Protoc*, 2017. **12**(6): p. 1198-1228.
5. Sharonov, A. and R.M. Hochstrasser, *Wide-field subdiffraction imaging by accumulated binding of diffusing probes*. *Proc Natl Acad Sci U S A*, 2006. **103**(50): p. 18911-6.
6. Hein, B., K.I. Willig, and S.W. Hell, *Stimulated emission depletion (STED) nanoscopy of a fluorescent protein-labeled organelle inside a living cell*. *Proc Natl Acad Sci U S A*, 2008. **105**(38): p. 14271-6.
7. Tröger, J., et al., *Comparison of Multiscale Imaging Methods for Brain Research*. *Cells*, 2020. **9**(6).
8. Zhao, Z., et al., *High-power homogeneous illumination for super-resolution localization microscopy with large field-of-view*. *Opt Express*, 2017. **25**(12): p. 13382-13395.
9. Mau, A., et al., *Fast widefield scan provides tunable and uniform illumination optimizing super-resolution microscopy on large fields*. *Nat Commun*, 2021. **12**(1): p. 3077.
10. Archetti, A., et al., *Waveguide-PAINT offers an open platform for large field-of-view super-resolution imaging*. *Nat Commun*, 2019. **10**(1): p. 1267.
11. Werbin, J.L., et al., *Multiplexed Exchange-PAINT imaging reveals ligand-dependent EGFR and Met interactions in the plasma membrane*. *Sci Rep*, 2017. **7**(1): p. 12150.
12. Xu, J., et al., *Super-resolution imaging reveals the evolution of higher-order chromatin folding in early carcinogenesis*. *Nat Commun*, 2020. **11**(1): p. 1899.
13. Creech, M.K., et al., *Superresolution Imaging of Clinical Formalin Fixed Paraffin Embedded Breast Cancer with Single Molecule Localization Microscopy*. *Sci Rep*, 2017. **7**: p. 40766.

14. Axelrod, D., *Cell-substrate contacts illuminated by total internal reflection fluorescence*. J Cell Biol, 1981. **89**(1): p. 141-5.
15. *Silicone Immersion Objectives Boost 3D Live-Cell Imaging*, in *BioPhotonics*. Olympus: https://www.photonics.com/Articles/Silicone_Immersion_Objectives_Boost_3D_Live-Cell/a62855.
16. Squires, T.M. and S.R. Quake, *Microfluidics: Fluid physics at the nanoliter scale*. Reviews of Modern Physics, 2005. **77**(3): p. 977-1026.
17. Civitci, F., et al., *Fast and multiplexed superresolution imaging with DNA-PAINT-ERS*. Nat Commun, 2020. **11**(1): p. 4339.
18. Arganda-Carreras, I., et al., *Trainable Weka Segmentation: a machine learning tool for microscopy pixel classification*. Bioinformatics, 2017. **33**(15): p. 2424-2426.
19. Eliceiri, K.W., et al., *Biological imaging software tools*. Nat Methods, 2012. **9**(7): p. 697-710.
20. Nan, X., et al., *Ras-GTP dimers activate the Mitogen-Activated Protein Kinase (MAPK) pathway*. Proc Natl Acad Sci U S A, 2015. **112**(26): p. 7996-8001.
21. Anderson, R.G. and K. Jacobson, *A role for lipid shells in targeting proteins to caveolae, rafts, and other lipid domains*. Science, 2002. **296**(5574): p. 1821-5.
22. Basu Roy, U.K., et al., *Caveolin-1 is a novel regulator of K-RAS-dependent migration in colon carcinogenesis*. Int J Cancer, 2013. **133**(1): p. 43-57.
23. Volonte, D., et al., *Caveolin-1 promotes the tumor suppressor properties of oncogene-induced cellular senescence*. J Biol Chem, 2018. **293**(5): p. 1794-1809.
24. Yang, G., et al., *Probing Electrolyte Solvents at Solid/Liquid Interface Using Gap-Mode Surface-Enhanced Raman Spectroscopy*. Journal of The Electrochemical Society, 2019. **166**(2): p. A178-A187.
25. Fuhrmann, D.C. and B. Brüne, *Mitochondrial composition and function under the control of hypoxia*. Redox Biol, 2017. **12**: p. 208-215.
26. Yu, M., et al., *Mitochondrial fusion exploits a therapeutic vulnerability of pancreatic cancer*. JCI Insight, 2019. **5**(16).
27. Prieto, J., et al., *Early ERK1/2 activation promotes DRP1-dependent mitochondrial fission necessary for cell reprogramming*. Nature Communications, 2016. **7**(1): p. 11124.
28. Yuen, A. and B. Díaz, *The impact of hypoxia in pancreatic cancer invasion and metastasis*. Hypoxia (Auckland, N.Z.), 2014. **2**: p. 91-106.
29. Smith, C.S., et al., *Fast, single-molecule localization that achieves theoretically minimum uncertainty*. Nat Methods, 2010. **7**(5): p. 373-5.
30. Przybylski, A., et al., *Gpufit: An open-source toolkit for GPU-accelerated curve fitting*. Sci Rep, 2017. **7**(1): p. 15722.
31. Li, L., et al., *Divide and conquer: real-time maximum likelihood fitting of multiple emitters for super-resolution localization microscopy*. Opt Express, 2019. **27**(15): p. 21029-21049.
32. Li, Y., et al., *Real-time 3D single-molecule localization using experimental point spread functions*. Nat Methods, 2018. **15**(5): p. 367-369.
33. Szymborska, A., et al., *Nuclear Pore Scaffold Structure Analyzed by Super-Resolution Microscopy and Particle Averaging*. Science, 2013. **341**(6146): p. 655-658.
34. Markus Mund, e.a., *Superresolution microscopy reveals partial preassembly and subsequent bending of the clathrin coat during endocytosis*. <https://www.biorxiv.org/content/10.1101/2021.10.12.463947v1>.
35. Mund, A., et al., *Deep Visual Proteomics defines single-cell identity and heterogeneity*. Nature Biotechnology, 2022.
36. Ouyang, W., et al., *Deep learning massively accelerates super-resolution localization microscopy*. Nature Biotechnology, 2018. **36**(5): p. 460-468.
37. Dember, L.M., *Amyloidosis-Associated Kidney Disease*. Journal of the American Society of Nephrology, 2006. **17**(12): p. 3458.
38. de Senneville, B.D., et al., *Deciphering tumour tissue organization by 3D electron microscopy and machine learning*. Communications Biology, 2021. **4**(1): p. 1390.

39. Riesterer, J.L., et al., *A workflow for visualizing human cancer biopsies using large-format electron microscopy*. bioRxiv, 2019: p. 675371.
40. Jacquemin, V., et al., *Dynamic Cancer Cell Heterogeneity: Diagnostic and Therapeutic Implications*. Cancers (Basel), 2022. **14**(2).
41. Marusyk, A., M. Janiszewska, and K. Polyak, *Intratumor Heterogeneity: The Rosetta Stone of Therapy Resistance*. Cancer Cell, 2020. **37**(4): p. 471-484.
42. Menyhárt, O. and B. Györfy, *Multi-omics approaches in cancer research with applications in tumor subtyping, prognosis, and diagnosis*. Comput Struct Biotechnol J, 2021. **19**: p. 949-960.
43. Allam, M., S. Cai, and A.F. Coskun, *Multiplex bioimaging of single-cell spatial profiles for precision cancer diagnostics and therapeutics*. NPJ Precis Oncol, 2020. **4**: p. 11.
44. Almada, P., et al., *Automating multimodal microscopy with NanoJ-Fluidics*. Nat Commun, 2019. **10**(1): p. 1223.
45. Klevanski, M., et al., *Automated highly multiplexed super-resolution imaging of protein nano-architecture in cells and tissues*. Nat Commun, 2020. **11**(1): p. 1552.
46. Lin, J.R., M. Fallahi-Sichani, and P.K. Sorger, *Highly multiplexed imaging of single cells using a high-throughput cyclic immunofluorescence method*. Nat Commun, 2015. **6**: p. 8390.
47. Agasti, S.S., et al., *DNA-barcoded labeling probes for highly multiplexed Exchange-PAINT imaging*. Chem Sci, 2017. **8**(4): p. 3080-3091.
48. Oleksiievets, N., et al., *Fluorescence lifetime DNA-PAINT for multiplexed super-resolution imaging of cells*. Commun Biol, 2022. **5**(1): p. 38.
49. Edelstein, A.D., et al., *Advanced methods of microscope control using μ Manager software*. J Biol Methods, 2014. **1**(2).
50. Nickerson, A., et al., *Photoactivated Localization Microscopy with Bimolecular Fluorescence Complementation (BiFC-PALM)*. J Vis Exp, 2015(106): p. e53154.